4-1-2013

Microbubble Cavitation Imaging

F. Vignon

W. T. Shi

J. E. Powers

E. Carr Everbach
Swarthmore College, ceverba1@swarthmore.edu

J. J. Liu

See next page for additional authors

Recommended Citation

F. Vignon, W. T. Shi, J. E. Powers, E. Carr Everbach, J. J. Liu, S. J. Gao, F. Xie, and T. R. Porter. (2013). "Microbubble Cavitation Imaging". *IEEE Transactions On Ultrasonics, Ferroelectrics, And Frequency Control*. Volume 60, Issue 4. 661-670. DOI: 10.1109/TUFFC.2013.2615
https://works.swarthmore.edu/fac-engineering/11

Published in final edited form as:
IEEE Trans Ultrason Ferroelectr Freq Control. 2013 April ; 60(4): 661–670. doi:10.1109/TUFFC.2013.2615.

Microbubble Cavitation Imaging

Francois Vignon, IEEE [Member],
Ultrasound, Photonics, and Bioinformatics, Philips Research USA, Briarcliff Manor, NY

William T. Shi, IEEE [Member],
Ultrasound, Photonics, and Bioinformatics, Philips Research USA, Briarcliff Manor, NY

Jeffry E. Powers,
R&D Investigations, Philips Medical Systems/ATL Ultrasound, Bothell, WA

E. Carr Everbach, IEEE [Member],
Department of Engineering, Swarthmore College, Swarthmore, PA

Jinjin Liu,
Cardiology Department, University of Nebraska Medical Center, Omaha, NE

Shunji Gao,
Cardiology Department, University of Nebraska Medical Center, Omaha, NE

Feng Xie, and
Cardiology Department, University of Nebraska Medical Center, Omaha, NE

Thomas R. Porter
Cardiology Department, University of Nebraska Medical Center, Omaha, NE

Francois Vignon: fancois.vignon@philips.com

Abstract

Ultrasound cavitation of microbubble contrast agents has a potential for therapeutic applications such as sonothrombolysis (STL) in acute ischemic stroke. For safety, efficacy, and reproducibility of treatment, it is critical to evaluate the cavitation state (moderate oscillations, stable cavitation, and inertial cavitation) and activity level in and around a treatment area. Acoustic passive cavitation detectors (PCDs) have been used to this end but do not provide spatial information.

This paper presents a prototype of a 2-D cavitation imager capable of producing images of the dominant cavitation state and activity level in a region of interest. Similar to PCDs, the cavitation imaging described here is based on the spectral analysis of the acoustic signal radiated by the cavitating microbubbles: ultraharmonics of the excitation frequency indicate stable cavitation, whereas elevated noise bands indicate inertial cavitation; the absence of both indicates moderate oscillations.

The prototype system is a modified commercially available ultrasound scanner with a sector imaging probe. The lateral resolution of the system is 1.5 mm at a focal depth of 3 cm, and the axial resolution is 3 cm for a therapy pulse length of 20 μs. The maximum frame rate of the prototype is 2 Hz. The system has been used for assessing and mapping the relative importance of the different cavitation states of a microbubble contrast agent. *In vitro* (tissue-mimicking flow phantom) and *in vivo* (heart, liver, and brain of two swine) results for cavitation states and their changes as a function of acoustic amplitude are presented.

I. Introduction

Terapeutic uses of microbubble (MB) ultrasound (US) contrast agents are emerging, notably for drug and gene delivery [1] and sonothrombolysis (STL) [2]. In the context of stroke, the

addition of US and MBs to standard thombolytic tissue plasminogen activator (tPA) therapy has been shown to accelerate thrombus dissolution in humans [3]. However, MB cavitation also has the potential for detrimental side effects under certain circumstances. Tung *et al*. [4] documented blood–brain barrier opening in mice at an acoustic peak negative pressure (PNP) of 0.3 MPa (generating dominant stable cavitation) and red blood cell extravasations at a PNP of 0.6 MPa (generating dominant inertial cavitation) at 1.5 MHz. These bioeffects may be dangerous in the presence of the anticoagulant and neurotoxic drug tPA. It is suspected that, in the presence of tPA, MB-mediated US even at relatively low PNPs (<0.3 MPa) can increase the occurrence rate of symptomatic hemorrhage in humans [5]. In addition, US and MBs alone (without tPA) have thrombolytic effects, as demonstrated in animal studies [6]–[8] and with a limited number of human subjects [9], without documented significant adverse effects. For the safety and effectiveness of a MB-mediated US treatment, the ultrasound power in the treatment region must be monitored and controlled. We hypothesize that the dynamic state of ultrasound-excited MBs in the treatment region is directly responsible for the therapy outcome and can be controlled by the local acoustic field. Therefore, it is essential to control and maintain a desirable type and level of MB cavitation in the treatment area inside the body for all patients. In particular, based on prior *in vitro* and *in vivo* experience, we hypothesized that stable cavitation is an efficient and safe regime for MB-mediated sonothrombolysis without tPA [8], [10], [11].

Particularly for MB-mediated US stroke therapy, it is important to adjust the acoustic output for the compensation of the individual skull attenuation because human skulls exhibit a wide range of patient-dependent acoustic attenuations [12], [13]. Single-element-transducer-based passive cavitation detectors (PCDs) have been used for this purpose [4], [14]–[16], but they do not provide information on the heterogeneous spatial distribution of cavitation activities. Passive two-dimensional cavitation mapping has been proposed for monitoring localized cavitation induced by high-intensity focused ultrasound (HIFU) pulses [17], [18], but the setup had a limited axial resolution because of the asynchrony between the therapy pulses and the monitoring device.

We developed a prototype STL system capable of therapy guidance and cavitation imaging. The system is a modified commercial US scanner iE33 with a sector imaging probe S5-1 (Philips Healthcare, Andover, MA). Cavitation imaging is based on the spectral analysis of acoustic signals radiated by the cavitating microbubbles [4], [19], [20]: ultraharmonics of the excitation frequency indicate stable cavitation (SC), whereas noise bands indicate inertial cavitation (IC). The present paper demonstrates the use of the system *in vitro* and *in vivo*.

II. Methods

A. STL and Cavitation Monitoring System

An iE33 imaging scanner is modified with additional capabilities of image guidance, sonothrombolysis treatment, therapy monitoring, and cavitation imaging.

1) Image Guidance and Therapy Monitoring—The STL system is capable of B-mode imaging for locating anatomical landmarks; Doppler and low-mechanical index (MI) contrast imaging for identifying a vessel occlusion and monitoring recanalization as therapy progresses, and verifying the presence of MBs in a treatment area before launching the STL pulse sequence.

2) Acoustic Conditions in STL Treatment Mode—In this mode, ensembles of four 1.6-MHz STL pulses of the same length (to be chosen between 5, 10, 20, or 44 μs) are transmitted into 19 directions within a 54° sector area. Two 1.7-μs background B-mode

pulses are interleaved between consecutive ensembles of 4 STL pulses. Additional 1.7-μs B-mode pulses are sent into the rest of a 90° sector. The pulse sequence per frame is depicted in Fig. 1. The pulse repetition frequency (PRF) is 8 kHz and the frame rate is adjustable up to 20 Hz. The active aperture of the S5-1 probe is ~2 × 1 cm and the transmit focal depth is 3.2 cm.

3) PNP Calibration—The output amplitude of the ultrasound system is controlled in 0.5-dB increments of the driving voltage. In a separate calibration experiment, hydrophone measurements (diameter 0.2 mm, Precision Acoustics Ltd., Dorchester, UK) of the PNP were performed at increasing driving voltages of the sonothrombolysis pulses. A 5-cm-thick tissue mimicking phantom (TMP) with a nominal attenuation of 0.49 dB/MHz/cm was inserted between the S5-1 probe and the hydrophone. Efforts were made to place the hydrophone at the lateral peak of PNP at a depth of 6 cm. These measurements are used throughout the paper to document nominally derated PNPs.

4) Cavitation Imaging Algorithm—Backscattered RF data are streamed from the scanner's signal path via a separate computer workstation through a custom set of additional RF capture boards. Data processing and display are performed in real-time using Matlab. The first and second STL pulses within each ensemble of four are first subtracted to eliminate stationary echo components (as a tissue-suppression step). Only the first and second pulses are used within each ensemble because each individual pulse induces significant bubble destruction [21]. The resulting RF data (corresponding to nonstationary signals, presumably scattered only from cavitating bubbles) is then band-pass filtered at the first ultraharmonic band ($1.5f_0$, where f_0 is the insonation center frequency), the second harmonic band ($2f_0$), and noise bands ($1.25f_0$ and $1.75f_0$). The band-pass filters' bandwidth is matched to that of the transmit pulse. An additional high-pass filter with cutoff at $1.25f_0$ is applied to the tissue-suppressed signal to encompass all cavitation activity signals. For any given location in the image, if the local ultraharmonic amplitude exceeds the noise amplitude by at least 3 dB, the corresponding image pixels are colored yellow, indicating dominant SC. If this is not the case and the noise level is within 10 dB of the second harmonic level, the corresponding pixels are colored red, indicating dominant IC. If bubble signals cannot be classified as SC or IC, corresponding pixels are colored green, indicating dominant moderate oscillations (MO). The brightness is modulated by the intensity of the high-pass filtered data. If the high-pass filtered data are below the user-defined dynamic range (always 15 dB in this manuscript), no color is displayed and the background grayscale B-mode image is displayed with a 40 dB dynamic range. A block diagram of the algorithm is shown in Fig. 2.

The average spectrum of the nonstationary RF data over the treatment area or a restricted region of interest (RO I) is also displayed for qualitative evaluation (in decibel scale, with a 60 dB dynamic range). Examples of the display available to the user during STL treatment are presented in Figs. 4–5 and 7–9. It is displayed side-to-side (on the workstation's screen) with the scanner's display of the B-mode image of the anatomy. Note that the B-mode images that underlie the cavitation images presented in this paper are of substantially lower quality than the standard (commercial) B-mode images produced by the scanner, because of the use of many fewer A-lines (44 versus 128 to 256 typically) and an incomplete signal and image processing chain (for speed in Matlab). An instantaneous cavitation dose was also calculated for each frame: the ultraharmonic and noise doses are the spatial averages of the ultraharmonic- and noise-filtered images, respectively, and are used as proxies for SC and IC strengths.

B. In Vitro Study

The commercially available US contrast agent Definity (Lantheus Medical Imaging, North Billerica, MA) is employed. The contrast MBs at a concentration of 0.01 mL/L are circulated in closed loop inside a 6-mm-diameter vessel phantom (model 524, ATS Laboratories, Bridgeport, CT) at 3 cm depth, using 14-mm-diameter tubing and a peristaltic pump set at 125 mL/min (Masterflex Digi-staltic model 77200–60, Cole-Parmer, Vernon Hills, IL). The imaging depth is 6 cm. The imaging rate is 2 Hz, allowing significant microbubble replenishment between consecutive images. The phantom is insonified longitudinally with 20-μs pulses, first through a coupling water path, then through the squama of three thin human temporal bone samples (<2 mm thickness, no trabecular bone present) to investigate the effects of frequency-dependent attenuation. A schematic of the experimental setup is presented in Fig. 3. Cavitation images were recorded at 2 Hz at increasing output MIs: every four frames, the probe's driving voltage was increased by 1 dB for an MI range of 0.1 to 1.7.

C. In Vivo Study

Animal studies were approved by the Institutional Animal Care and Use Committee at University of Nebraska Medical Center (UNMC).

Two pigs (weight ~35 kg) were anesthetized with isoflurane and ventilated at 10 breaths per minute. Intravenous (IV) lines were placed for MB infusion. One vial was diluted in 0.9% normal saline (3% Definity) and infused over 30 min at an average rate of 3 mL/min. The STL system was synchronized to the animals' ECG signals (one image every 2 heart beats; that is, an imaging rate of ~0.8 Hz at 100 heart beats per minute). This allowed sufficient bubble replenishment for comparable bubble concentrations from image to image in the main arteries. 20-μs-long STL pulses were used. The imaging depth was 6 cm. Cavitation images were displayed and recorded at increasing MIs: the scanner's output voltage was increased every 4 frames by 1 dB for an MI range of 0.1 to 1.7. For each pig, two data sets were acquired for three organs: brain (transtemporally), heart (parasternal short-axis view of the left ventricle), and liver (subcostal view, no respiration gating). The brain and heart views correspond to views typically used in brain and heart sonothrombolysis studies at UNMC [8], [11].

III. Results

A. In Vitro Study

1) Cavitation Imaging—Example cavitation images of the vessel phantom are shown in Fig. 4 (skull sample not inserted) and Fig. 5 (skull sample inserted under the S5-1 probe). Spatial information is provided showing cavitation activities confined within the vessel, and at higher cavitation levels toward the center of the image than at the edges (reflecting angle-dependent transmission power of the phased array and refraction effects at the skull interface [22]). Signal smears beyond the vessel boundaries resulting from the poor spatial resolution (at best 3 cm for a 20-μs pulse length). In both cases (without and with skull), cavitation imaging allows visualizing the transitions between dominant MO, SC, and IC as pulse amplitude is increased. Notice that in this particular case, no strong frequency-dependent attenuation effects (as would be expected when transmitting ultrasound through skull) are observed; this may be due to the thinness of this particular bone sample (<2 mm of cortical bone).

2) Dose Monitoring and Skull Attenuation—By displaying the average spectrum of the backscattered signal over a region of interest as a function of MI, the user can visualize at which MIs dominant SC and dominant IC occur. Fig. 6 (left) shows the spectrum

evolution as a function of MI through water (top) and through a temporal bone sample (bottom). In the nonattenuated experiment, salient ultraharmonics (indicating dominant SC) are clearly seen from MIs ~0.3 to 0.8 and strong noise (indicating dominant IC) occurs from MIs ~0.8 to 1.5. At higher MIs, both the ultraharmonic and noise responses fade, which may be indicative of a higher regime of fast bubble destruction. Through the temporal bone sample, salient ultraharmonics are seen starting at an MI of ~0.9 and no dominant noise can be seen up to an MI of 1.7.

It is possible to quantitatively identify the threshold for dominant stable cavitation from the recorded back-scattered spectra and cavitation doses (Fig. 6, right). The threshold is defined as the MI value at which the ultraharmonic dose exceeds the noise dose by at least 3 dB, indicating salient ultraharmonic activity. By comparing the MI threshold for SC through a skull sample to the threshold through an unattenuated path, it is possible to estimate the attenuation of the skull sample noninvasively (that is, without the need to use a hydrophone on the other side of the skull). With a 20-μs pulse length, the SC threshold is measured at MI = 0.3 through an unattenuated path, and MIs of 0.6, 0.7, and 0.9 through three temporal bone samples. These values correspond to estimates of 50% to 66% bone attenuation. This is below reported values in the literature (averaging ~80% attenuation at 2 MHz) [12], [13] but can be explained by the observed thinness and absence of trabecular bone of the tested samples, and the lower frequency. The thresholds vary slightly as a function of pulse length, with longer pulses corresponding to lower MI thresholds [23].

B. In Vivo Study

1) Cavitation Imaging—*In vivo* cavitation images of the brain, heart, and liver from one of the two imaged pigs are shown in Figs. 7, 8, and 9, respectively. In both pigs, cavitation imaging allowed visualization of the transitions between dominant MO, SC, and IC. However, the transitions were not as sharp as seen *in vitro*, so that it was difficult to establish clear threshold values between cavitation regimes, with the exception of cavitation within the heart left ventricle. Most of the time, the cavitation image showed a mix of two or three of the cavitation regimes present at the same time in the treatment area. The image also varied significantly from one image to the next (i.e., from one cardiac cycle to the next; see videos), probably because of threshold effects on the changing bubble populations. In the liver images, respiratory motion was an additional cause of variability. Spatial information is provided showing dominant cavitation activities confined around major vessels in the brain and liver and within the ventricle in the heart image. Signal smearing in the axial dimension was problematic, with signals appearing to originate from beyond the contralateral skull in the brain images. For the heart, signal smearing from the relatively high-bubble-concentration areas in the ventricle into the low-bubble-density myocardium make it virtually impossible to monitor cavitation activities in the myocardium.

2) Dose Monitoring—Fig. 10 (left) displays the back-scattered spectra from the RO I as a function of MI in the brain (top), heart (middle), and liver (bottom). For a given organ, similar patterns were observed in both pigs.

Fig. 10 (right) shows the corresponding ultraharmonic and noise doses as a function of MI. Only in the case of microbubbles in the left ventricle is it possible to reliably identify the SC threshold (the MI at which the ultraharmonic dose exceeds the noise dose by at least 3 dB) at an MI of 0.6. The heart is a special case, with a high concentration of freely oscillating bubbles in the large heart chamber, resulting in a high SNR for cavitation monitoring.

IV. Discussion

An imaging transducer was used to deliver sonothrombolysis pulses and spatially and temporally monitor the dominant state and activity level of cavitation present in a treatment area. The system was demonstrated *in vitro* and *in vivo*.

Earlier versions of this microbubble cavitation imaging system have been used successfully to correlate therapeutic safety and efficacy to cavitation state and activity level in *in vitro* [10] and *in vivo* [8], [11] studies. In the absence of tPA, a moderate level of SC was as effective as IC for *in vitro* thrombus dissolution [10] but the stronger IC levels seemed to be required for consistent recanalization *in vivo* in a pig ischemic brain model [8]. In the presence of tPA, SC seemed more effective than IC in a cardiac ischemia model [11]. In our experience, it seems that in the absence of tPA, moderate levels of IC may be more effective than SC without causing harmful bioeffects [8].

In the future, when the optimal cavitation state and level are firmly established, it is expected that microbubble cavitation imaging can be used to plan and monitor therapy and ensure that each patient receives the adequate cavitation dose, adaptively modulating the ultrasound output power to compensate from patient-dependent skull attenuation effects.

The 2 Hz frame rate of the cavitation imaging mode is currently suboptimal for cavitation monitoring but sufficient for treatment planning: acquiring cavitation dose curves as a function of MI such as those in Fig. 6 and 10 takes less than 1 min. This procedure allows the user to decide which output MI is required for a desired cavitation state before starting the actual therapy. Note that 2 Hz, or one image every other heartbeat, seems to be slightly too fast to allow new bubbles to completely replenish the insonified area in the phantom and animal experiments, respectively. This would account for the plateau observed in the cavitation curves at higher MIs.

Cavitation monitoring during STL treatment also allows estimating the rate at which MBs are destroyed. *Post hoc* analysis from a pig STL study suggests that at the MIs used in the study (1.7 and 2.4) most MBs are destroyed in only one frame (50 ms), so that the bubble duty cycle is, in effect, much shorter than the ultrasound duty cycle [21]. This measurement tool may enable fine-tuning of pulse sequences according to local bubble replenishment rate for optimal use of the MBs, e.g., guiding how long to apply the therapeutic impulses.

Engineering work remains to improve the algorithm for robustness. For example, although ultraharmonics were clearly seen *in vitro* and transthoracically in the heart left ventricle *in vivo*, their visualization was often problematic in the brain and liver. Possible solutions include working with a higher MB dose, a more homogeneous MB formulation (different MB sizes in the field of view may be subjected to different cavitation states and levels under the same ultrasound excitation), modifying the central frequency for more efficient generation of SC (because the cavitation state and level as a function of pressure are frequency-dependent), lowering the central frequency for better transcranial and tissue penetration, using temporally apodized waveforms to prevent spectral side lobes, compensating for frequency-dependent effects caused by the transducer bandwidth and skull and tissue attenuation, and utilizing autoregression analysis or wavelet analysis for more sensitive spatio-temporal detection of the ultraharmonic component and principal component analysis for more accurate cavitation state classification. Finally, the green-yellow-red display of cavitation intensities relies on user-defined thresholds and results in discontinuities in the image. Classifying a given pixel inside one of three cavitation regimes is also not representative of the reality of a cavitation field in which several cavitation states usually exist simultaneously in proximity because of a wide distribution of bubble sizes,

bubble environment (e.g., within a capillary versus within a large artery), and spatially heterogeneous acoustic field. Other display solutions thus remain to be investigated. For example, it may be a better alternative to display separate SC or IC probability maps rather than to show information of all three cavitation modes on one single display, and a state-of-the art display solution should be implemented, such as that suggested in [24].

Spatio-temporal cavitation imaging also suffers from fundamental limitations. First, the poor axial resolution precludes precise identification of the origin of the cavitation signals. For example, microcirculation cavitation cannot be separated from cavitation from nearby major arteries (or the heart chambers) because of signal smearing from these larger pools of contrast microbubbles that probably contribute to most of the observed cavitation signals. Shorter pulses yield better resolution but less robust cavitation states—because several cycles of ultrasound are typically needed before stable cavitation can be observed—and poorer spectral resolution. In our experience, the shortest pulse length at which ultraharmonics have been confidently observed was 10 μ s (corresponding to an axial resolution of 1.5 cm) [23]. Another reason why it is difficult to estimate microcirculation cavitation in our study was that the time interval between frames did not allow for replenishment of bubbles within the microcirculation (typically of the order of several seconds). In sonothrombolysis for acute ischemic stroke treatment, the target is a blood clot in a major artery of the brain (a few millimeters in diameter) and cavitation within those vessels can probably be resolved, but further work is required to address cavitation monitoring in the microcirculation.

Second, subtraction of consecutive pulses is necessary to eliminate tissue interference, but results in nonlinear estimates of cavitation intensity. Also, the bubble signal is highly variable from one frame to the next because there is a significantly new bubble population in each frame at this low frame rate, and because of significant bubble destruction. The resulting temporal discontinuities may be mitigated by higher frame-rate imaging or at lower insonation pressures.

Finally, the observed evolution of the backscattered spectra was more complicated than our simplified hypothesis of three distinct cavitation modes separated by MI thresholds. Through the skull, high levels of broadband electronic noise were present at very low MIs because of low SNR resulting from high attenuation, yielding a false display of dominant IC. In some situations, ultraharmonics were barely visible; in others there seemed to be two successive ultraharmonic regimes (see, e.g., the nonattenuated *in vitro* experiment of Fig. 6 (top): ultraharmonics first are present with little background noise at MIs of 0.3 to 0.8, then the ultraharmonics are indistinguishable from the noise from MIs of 0.8 to 1.0, and at higher MIs, salient ultraharmonics appear again, this time concurrently with elevated noise. In the green-yellow-red display, this shows as a pure yellow display (MIs 0.3 to 0.8), followed by pure red (0.8 to 1.0) followed by a mix of yellow and red (1.0 and higher). It is also notable that in most experiments the relative level of noise (with respect to the fundamental) starts to increase at low MIs, then peaks and decreases at higher MIs. This may be indicative of a faster destruction rate of the microbubbles, but it may also be an artifact resulting from the tissue suppression part of the algorithms, in which the data from two consecutive pulses are subtracted. It has also been observed that the second harmonic value (normalized to the fundamental) tends to peak at about the value of the SC threshold, then decreases at higher MIs. These observations pose fundamental questions about the physical mechanisms that are the cause of the observed spectral patterns, presenting challenges to microbubble cavitation imaging. It is likely that the analysis of the entire spectrum (and not only a few of its features: ultraharmonics, second harmonics, and broadband noise strength, as presented here) should be utilized for classifying dominant cavitation regimes.

V. Conclusion

An ultrasound imaging system was modified to deliver sonothrombolysis pulses and spatially and temporally monitor the dominant state and level of cavitation activity present in a treatment area. Such a tool will be useful in advancing the understanding of cavitation mechanisms in sonothrombolysis and other MB-mediated US therapies. It is hoped that this tool will allow safe and effective thrombolysis treatment: cavitation imaging enables treatment planning (estimating skull attenuation and compensating for it by adjusting the output power) and monitoring (generating and updating 2-D cavitation maps).

References

1. Mayer CR, Geis NA, Katus HA, Bekeredjian R. Ultrasound targeted microbubble destruction for drug and gene delivery. Expert Opin. Drug Deliv. 2008; vol. 5(no. 10):1121–1138. [PubMed: 18817517]
2. Meairs S, Culp W. Microbubbles for thrombolysis of acute ischemic stroke. Cerebrovasc. Dis. 2009; vol. 27(suppl. 2):55–65. [PubMed: 19372661]
3. Tsivgoulis G, Eggers J, Ribo M, Perren F, Saqqur M, Rubiera M, Sergentanis TN, Vadikolias K, Larrue V, Molina CA, Alexandrov AV. Safety and efficacy of ultrasound-enhanced thrombolysis: a comprehensive review and meta-analysis of randomized and nonrandomized studies. Stroke. 2010; vol. 41(no. 2):280–287. [PubMed: 20044531]
4. Tung YS, Vlachos F, Choi JJ, Deffieux T, Selert K, Konofagou EE. In vivo transcranial cavitation threshold detection during ultrasound-induced blood–brain barrier opening in mice. Phys. Med. Biol. 2010; vol. 55(no. 20):6141–6155. [PubMed: 20876972]
5. Molina CA, Barreto AD, Tsivgoulis G, Sierzenski P, Malkoff MD, Rubiera M, Gonzales N, Mikulik R, Pate G, Ostrem J, Singleton W, Manvelian G, Unger EC, Grotta JC, Schellinger PD, Alexandrov AV. Transcranial ultrasound in clinical sonothrombolysis (TUCSON) trial. Ann. Neurol. 2009; vol. 66(no. 1):28–38. [PubMed: 19670432]
6. Xie F, Tsutsui JM, Lof J, Unger EC, Johanning J, Culp WC, Matsunaga T, Porter TR. Effectiveness of lipid microbubbles and ultrasound in declotting thrombosis. Ultrasound Med. Biol. 2005; vol. 31(no. 7):979–985. [PubMed: 15972204]
7. Xie F, Lof J, Everbach C, He A, Bennett RM, Matsunaga T, Johanning J, Porter TR. Treatment of acute intravascular thrombi with diagnostic ultrasound and intravenous microbubbles. JACC Cardiovasc. Imaging. 2009; vol. 2(no. 4):511–518. [PubMed: 19580735]
8. Shi, WT.; Vignon, F.; Powers, JE.; Gao, S.; Liu, J.; Xie, F.; Drvol, L.; Lof, J.; Everbach, EC. Investigation of image-guided sonothrombolysis in a porcine acute ischemic stroke model; 2011 IEEE Int. Ultrasonics Symp; p. 5-8.
9. Seidel G. Transcranial ultrasound therapy in patients ineligible for tPA. Cerebrovasc. Dis. 2008; vol. 26(suppl 1):1–20.
10. Shi, WT.; Gao, S.; Vignon, F.; Powers, JE.; Drvol, L.; Jung, KW.; Xie, F.; Lof, J.; Everbach, EC.; Porter, TR. In vitro investigation of effectiveness of microbubble stable cavitation in thrombolysis; 2010 IEEE Int. Ultrasonics Symp; p. 330-333.
11. Xie F, Gao S, Wu J, Unger E, Liu J, Shi WT, Vignon F, Powers J, Lof J, Kutty S, Porter T. Prospective randomized comparison of long versus short pulse duration therapeutic impulses in improving epicardial and microvascular recanalization during a continuous microbubble infusion in acute myocardial infarction. J. Am. Coll. Cardiol. 2012; vol. 59 suppl(no. 13):E1132.
12. Hölscher T, Wilkening WG, Molkenstruck S, Voit H, Koch C. Transcranial sound field characterization. Ultrasound Med. Biol. 2008; vol. 34(no. 6):973–980. [PubMed: 18255216]
13. Ammi AY, Mast TD, Huang IH, Abruzzo TA, Coussios CC, Shaw GJ, Holland CK. Characterization of ultrasound propagation through ex vivo human temporal bone. Ultrasound Med. Biol. 2008; vol. 34(no. 10):1578–1589. [PubMed: 18456391]
14. Madanshetty SI, Roy RA, Apfel RE. Acoustic microcavitation: Its active and passive acoustic detection. J. Acoust. Soc. Am. 1991; vol. 90(no. 3):1515–1526. [PubMed: 1939908]

15. Everbach EC, Makin IR, Azadniv M, Meltzer RS. Correlation of ultrasound-induced hemolysis with cavitation detector output in vitro. Ultrasound Med. Biol. 1997; vol. 23(no. 4):619–624. [PubMed: 9232771]

16. Accredited Standards Committee on Acoustics. ANSI. Washington, DC: 2010. Bubble detection and cavitation monitoring. ANSI S1.24 TR-2002

17. Jensen CR, Ritchie RW, Gyöngy M, Collin JR, Leslie T, Coussios CC. Spatiotemporal monitoring of high-intensity focused ultrasound therapy with passive acoustic mapping. Radiology. 2012 Jan.vol. 262:252–261. [PubMed: 22025731]

18. Salgaonkar VA, Datta S, Holland CK, Mast TD. Passive cavitation imaging with ultrasound arrays. J. Acoust. Soc. Am. 2009 Dec; vol. 126(no. 6):3071–3083. [PubMed: 20000921]

19. Datta S, Coussios CC, Ammi AY, Mast TD, de Courten-Myers GM, Holland CK. Ultrasound-enhanced thrombolysis using Definity as a cavitation nucleation agent. Ultrasound Med. Biol. 2008; vol. 34(no. 9):1421–1433. [PubMed: 18378380]

20. Coussios CC, Farny CH, Haar GT, Roy RA. Role of acoustic cavitation in the delivery and monitoring of cancer treatment by high-intensity focussed ultrasound. Int. J. Hyperthermia. 2007; vol. 23(no. 2):105–120. [PubMed: 17578336]

21. Vignon, F.; Shi, W.; Liu, J.; Xie, F.; Gao, S.; Drvol, L.; Lof, J.; Everbach, C.; Porter, T.; Powers, J. In vivo microbubble cavitation imaging; 2011 IEEE Ultrasonics Symp; p. 927-930.

22. Vignon F, Shi WT, Yin X, Hoelscher T, Powers JE. The stripe artifact in transcranial ultrasound imaging. J. Ultrasound Med. 2010; vol. 29(no. 12):1779–1786. [PubMed: 21098850]

23. Vignon, F.; Shi, WT.; Powers, JE.; Liu, J.; Drvol, L.; Lof, J.; Everbach, C.; Gao, S.; Xie, F.; Porter, T. Real-time two-dimensional imaging of microbubble cavitation; Proc. 11th Int. Symp. Therapeutic Ultrasound; 2011. p. 407-413.

24. Borland D, Taylor MR 2nd. Rainbow color map (still) considered harmful. IEEE Comput. Graph. Appl. 2007; vol. 27(no. 2):14–17. [PubMed: 17388198]

Biographies

Francois Vignon (M’06) was born in Paris, France, in 1978. He received M.Sc. degrees in both physics and natural sciences from ENS Paris in 2001 and 2002, and a Ph.D. degree in physics from ESPCI-Paris Tech in 2005. After a short postdoctoral experience in satellite image processing at Ecole Polytechnique de Paris, he joined Philips Research North America as a Senior Researcher in 2006. His research interests include beamforming, signal and image processing, ultrasound interventional guidance, transcranial imaging, contrast agents, and sonothrombolysis.

William T. Shi (M’01) received a B.Sc. degree in physics in 1983 and an M.Sc. degree in applied physics in 1986, both from Nanjing University; he received M.Sc. and Ph.D. degrees in engineering from Yale University in 1992 and 1995, respectively. He was an assistant lecturer and then lecturer of acoustics at Nanjing University from 1986 to 1989. After

postdoctoral training at Emory University, Dr. Shi became an assistant and then associate professor of radiology at Thomas Jefferson University during 1996 to 2002. Afterward, he was recruited to GE Ultrasound as a senior systems engineer. Since 2004, Dr. Shi has been a corporate researcher at Philips Research. His research interests include: sonothrombolysis, ultrasound contrast imaging, transcranial ultrasound imaging, cavitation with contrast microbubbles, ultrasound-mediated drug delivery, contrast-assisted blood pressure and flow velocity estimation, nonlinear ultrasound properties of biological tissues, and dynamics and instabilities of liquid interfaces.

Jeffry E. Powers was born in Santa Monica, CA, in 1950. He received a B.A. degree in physics in 1972 and an M.S. degree in bioengineering in 1974, both from the University of California, San Diego; he earned a Ph.D. degree in electrical engineering in 1980 from the University of Washington. After a 1-year postdoctoral fellowship at Kantonsspital Basel, Switzerland, in 1982, he joined Advanced Technology Laboratories, where he led the development of color flow imaging. He began working on ultrasound contrast imaging in 1991; since then, has been involved with various aspects, including imaging and sonothrombolysis.

E. Carr Everbach (M’90) received his A.B. degree in mechanics/acoustics in 1982 from Harvard College; he received his M.S. and Ph.D. degrees in mechanical engineering in 1986 and 1989, respectively, from Yale University, where he studied biomedical acoustics under Robert Apfel. A Hunt Fellow of the Acoustical Society of America and a 1992 NSF Presidential Faculty Fellow, his research areas include quantification of acoustic cavitation, nonlinear propagation, and bubble physics. He has taught engineering at Swarthmore College since 1990.

Jinjin Liu was born in November 1982, in Hunan, China. He received his B.S. and M.S degrees from the Department of Physics and the Faculty of Materials, Optoelectronics, and Physics at Xiangtan University, Hunan, China, in 2004 and 2007, respectively. Currently, he is a Ph.D. candidate in the Department of Engineering Mechanics of the University of Nebraska–Lincoln, Lincoln, NE. His research interests include finite element analysis for acoustic, vibration, piezoelectrics, and thermodynamics, as well as applications of diagnostic and therapeutic ultrasound. He is a member of the Chinese American Heart Association.

Shunji Gao was born in Quanzhou, Fujian Province, China, in 1978. He received his M.D. degree in 2002 from Southern Medical University in Guangzhou. He was a resident of Wuhan General Hospital at Wuhan, Hubei Province, and then a postgraduate fellow of the Third Military Medical University in Chongqing, China, from 2002 to 2009. Dr. Gao completed a two-year postdoctoral training at the University of Nebraska Medical Center during 2009 through 2011. Since then, he has been an attending doctor of Wuhan General

Hospital. His research interests include microbubble-enhanced ultrasonography, transcranial ultrasound imaging and sonothrombolysis for acute myocardial infarct and ischemia stroke treatment, and drug-carrying microbubbles and their localized ultrasonic delivery for cancer therapy.

Feng Xie was born in Nanjing, China, in 1954. He graduated from the Jiamusi Medical School in 1975. His cardiology training took place at the Chinese PLA Postgraduate Medical School from 1982 to 1985. He went to the University of Rochester Medical Center for an advanced postdoctoral training from 1986 to 1987. He became an associate professor and vice director in the Department of Diagnostic Ultrasound at the Chinese PLA General Hospital in 1990. In 1992, he was a visiting professor at the University of Pennsylvania Medical Center. He worked at the University of Nebraska Medical Center as a research associate and instructor from 1993 to 1995. In 1996, he was appointed as a Chief of Department of Ultrasound at the Chinese Cardiovascular Institute and Fuwai Heart Hospital, Peking Union Medical College and Chinese Medical Academy. He is currently an associate professor of medicine at the University of Nebraska Medical Center.

Dr. Xie's research interests are cardiac imaging and therapeutic ultrasound with microbubbles in coronary heart diseases.

He is a member of the American Heart Association and the American Society of Echocardiography. He served as a reviewer for the *American Journal of Cardiology*, the *Journal of the American Society of Echocardiography*, and the *American Heart Journal*.

Thomas R. Porter obtained his M.D. degree from the University of Nebraska in 1984 and completed residency in Internal Medicine and Fellowship in Cardiology, both at the Medical College of Virginia, in 1988 and 1991. He is currently professor of medicine and courtesy professor of radiology and pediatric cardiology as well as Theodore Hubbard chair of Cardiology at the University of Nebraska Medical Center (UNMC). He is also the director of the Non-Invasive Cardiology Laboratory at UNMC and a member of the Department of Internal Medicine Research Committee.

His research interests include using ultrasound contrast agents for clinical cardiac imaging and therapy, including sonothrombolysis for acute ischemia of the heart and brain.

Dr. Porter has received awards from the American College of Cardiology, the American Society of Echocardiography, and, in 2002, the Joseph P. Gilmore Outstanding Investigator award.

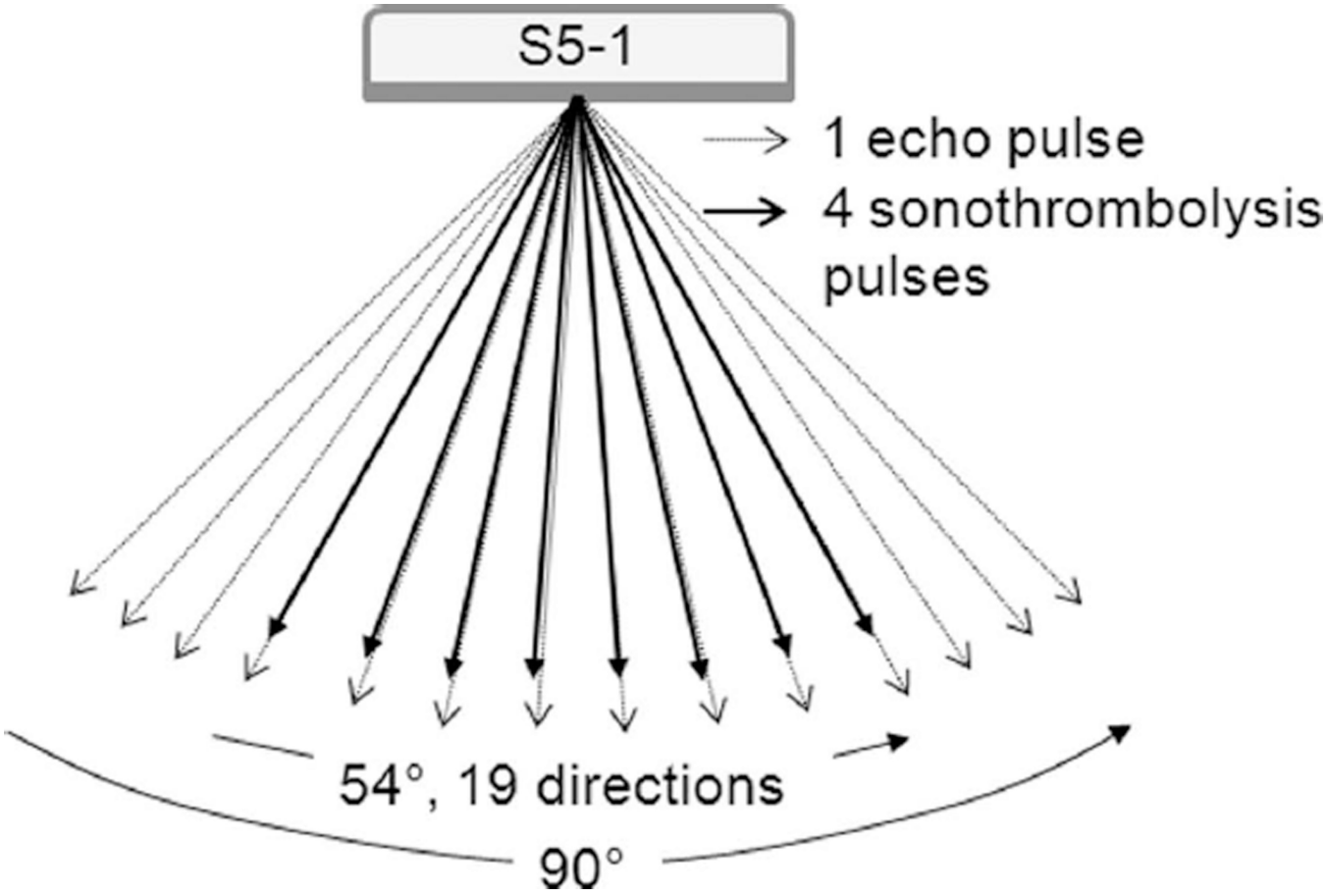

Fig. 1.
Sonothrombolysis (STL) pulse sequence. The STL pulses are sent as ensembles of 4 pulses of the same length. Short B-mode pulses of lower amplitude are interleaved to generate a background image of the anatomy.

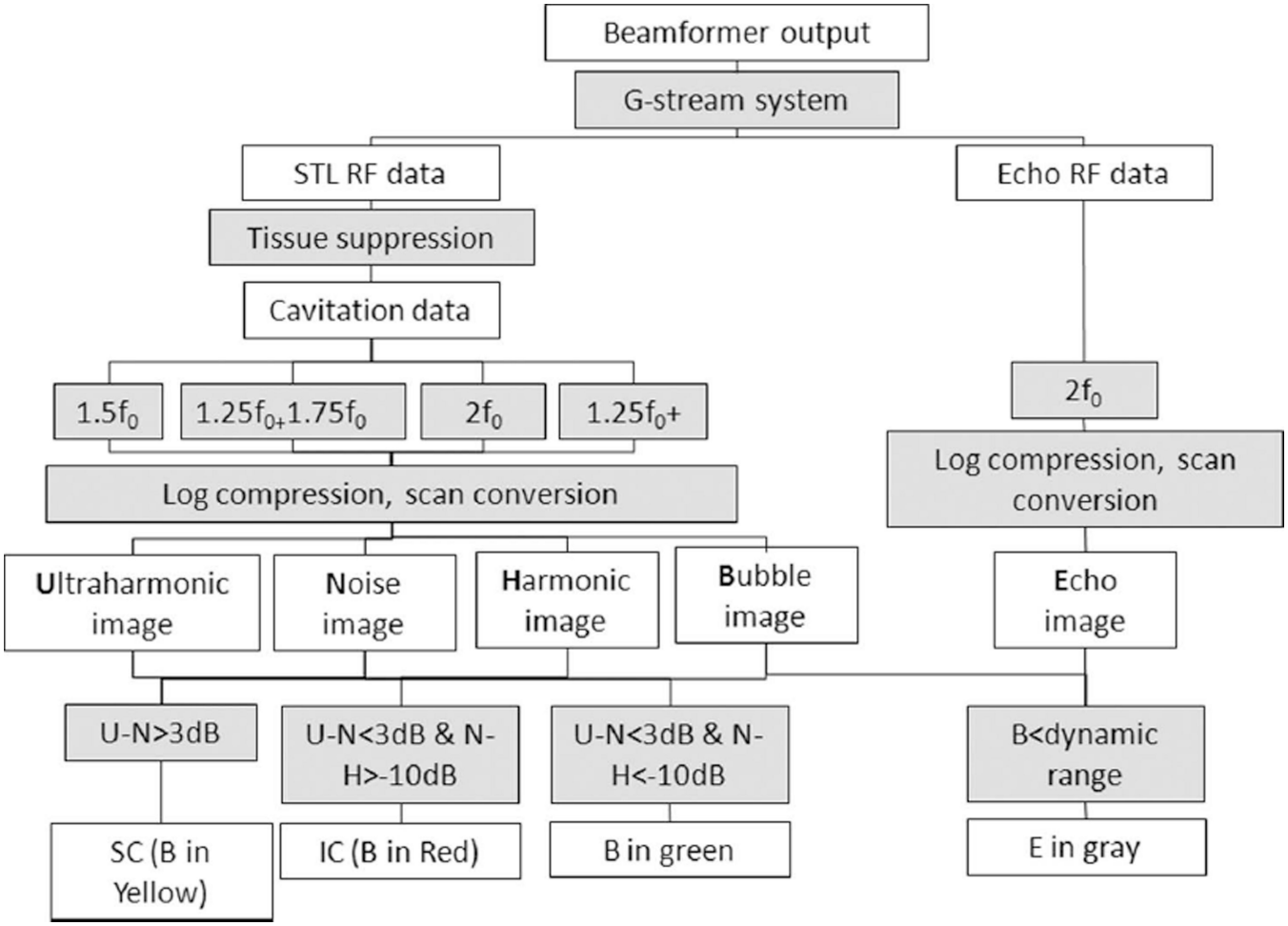

Fig. 2.
Block diagram of the cavitation imaging algorithm.

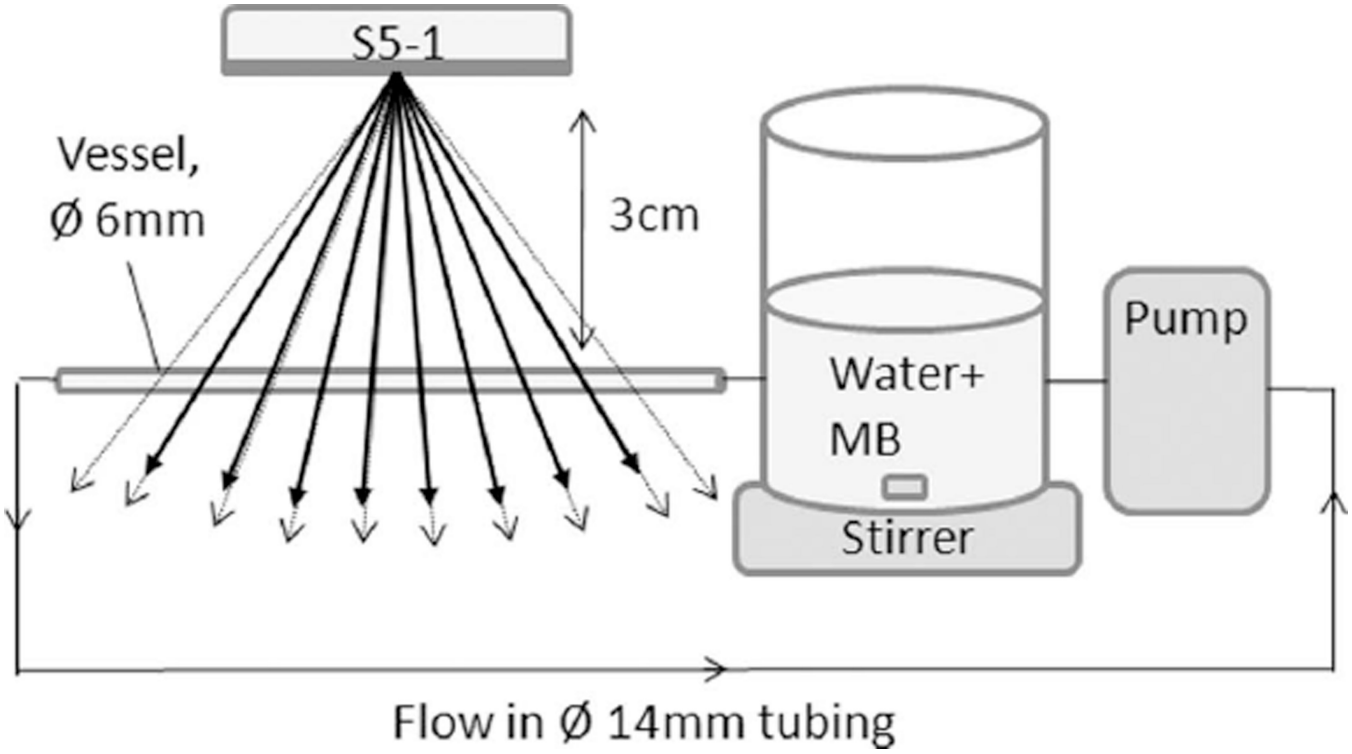

Fig. 3.
Schematic of the setup for *in vitro* experiments.

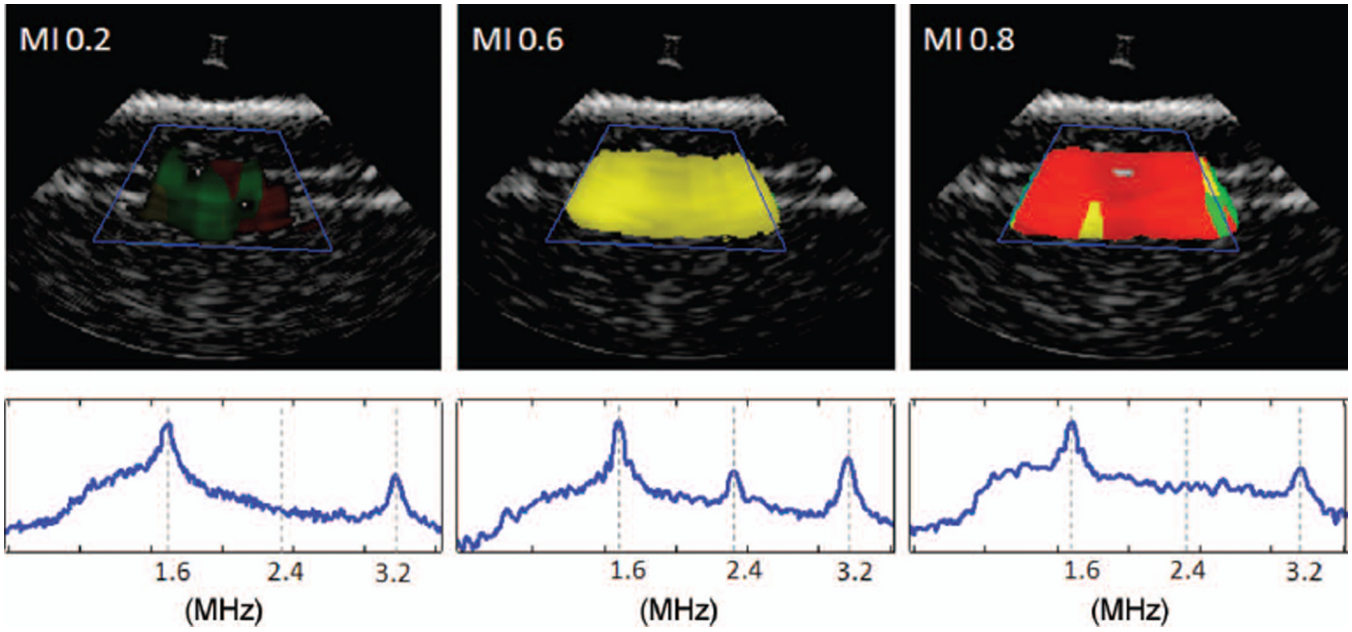

Fig. 4.

Cavitation images of a vessel phantom through a water path at mechanical indexes (MIs) with dominant moderate oscillations (left), dominant stable cavitation (center), and dominant inertial cavitation (right). The corresponding MIs are indicated, and the average spectrum over the region of interest outlined in blue is displayed in logarithmic scale.

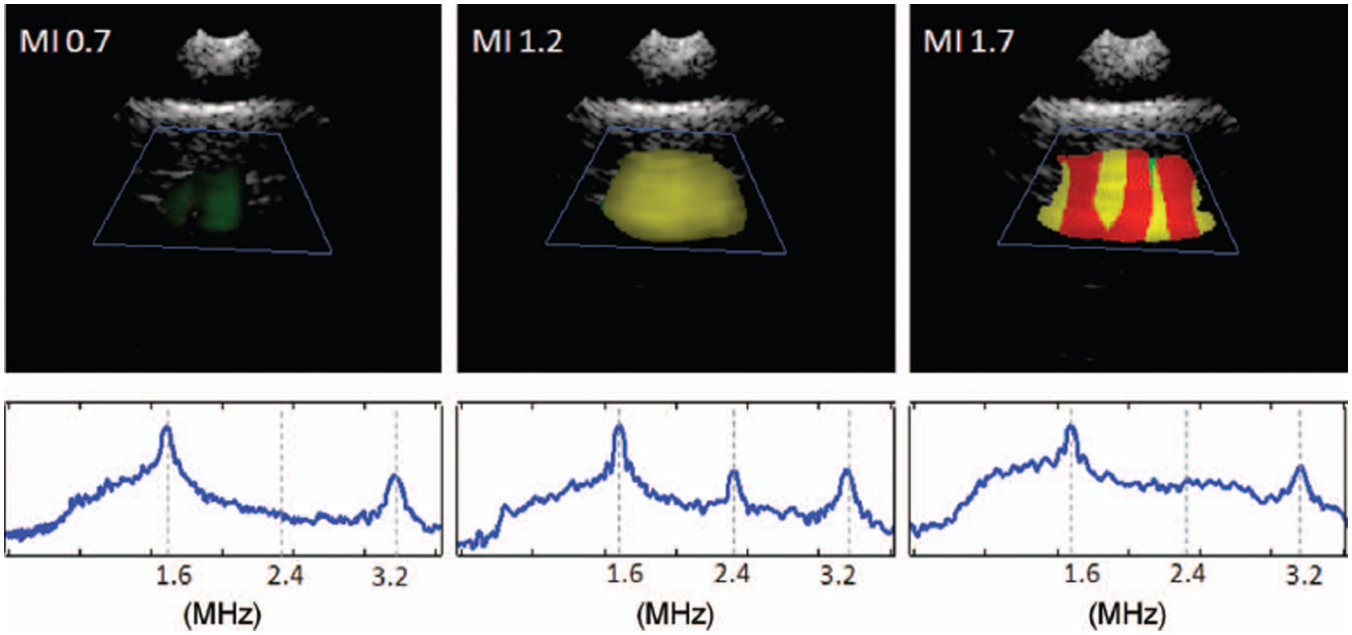

Fig. 5.

Cavitation images of a vessel phantom through a human temporal bone sample at mechanical indexes (MIs) with dominant moderate oscillations (left), dominant stable cavitation (center), and dominant inertial cavitation (right). The corresponding MIs are indicated, and the average spectrum over the region of interest outlined in blue is displayed in logarithmic scale.

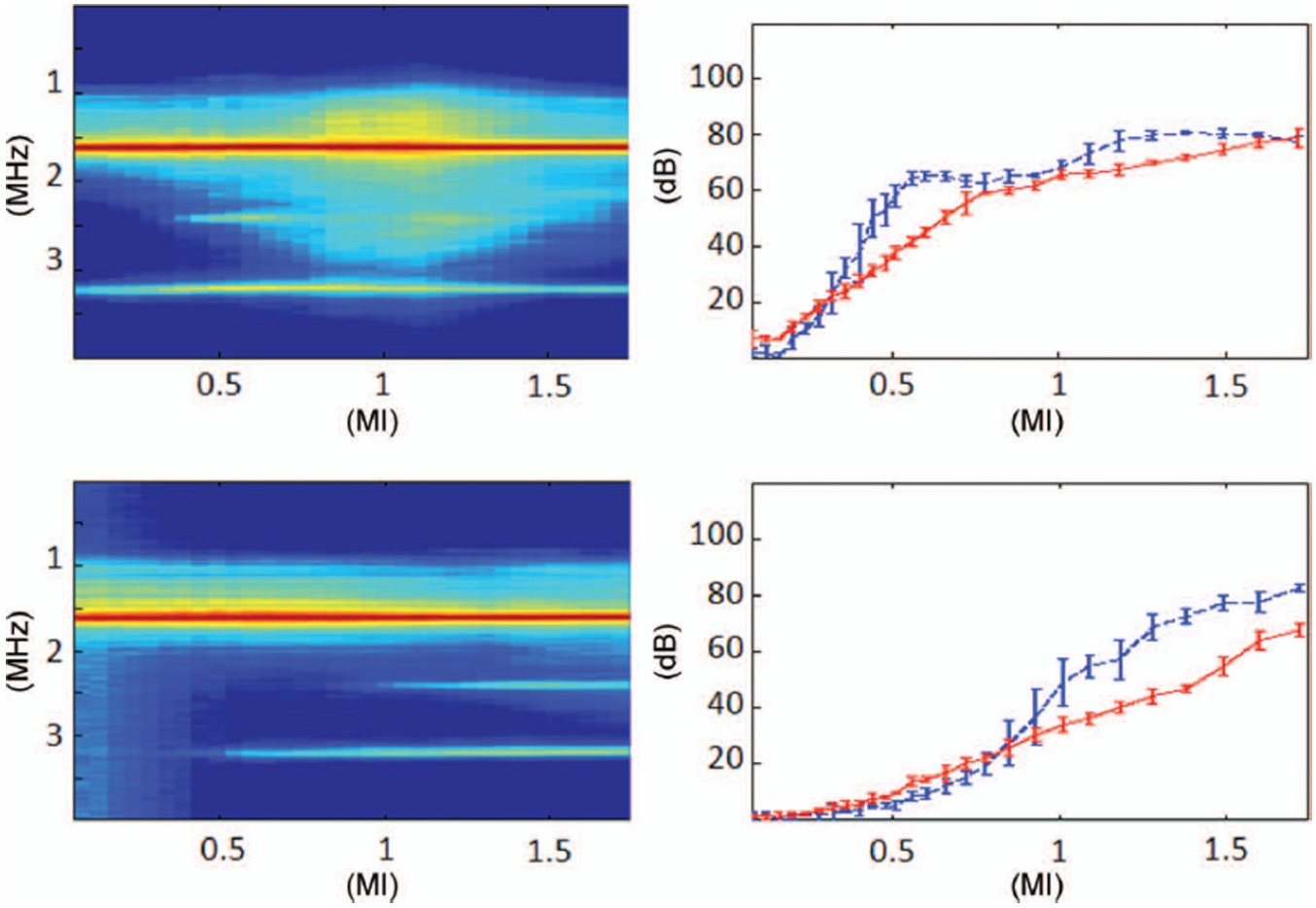

Fig. 6.

Averaged cavitation spectra (left) and cavitation doses (right) as a function of mechanical index (MIs), through water without a temporal bone (top) and through a temporal bone sample (bottom). Four measurements are taken at each MI. The spectra are averaged from the regions of interest (within the blue boxes) of Figs. 4 and 5 and displayed in a decibel scale (normalized to the fundamental frequency, 35 dB dynamic range). The cavitation doses (dashed blue for ultraharmonic, red for noise) are spatially averaged from the ROIs and displayed with error bars representing standard deviation over 4 measurements. The thresholds for stable cavitation (the ultraharmonic dose exceeds the noise dose by at least 3 dB) are indicated as vertical dashed lines.

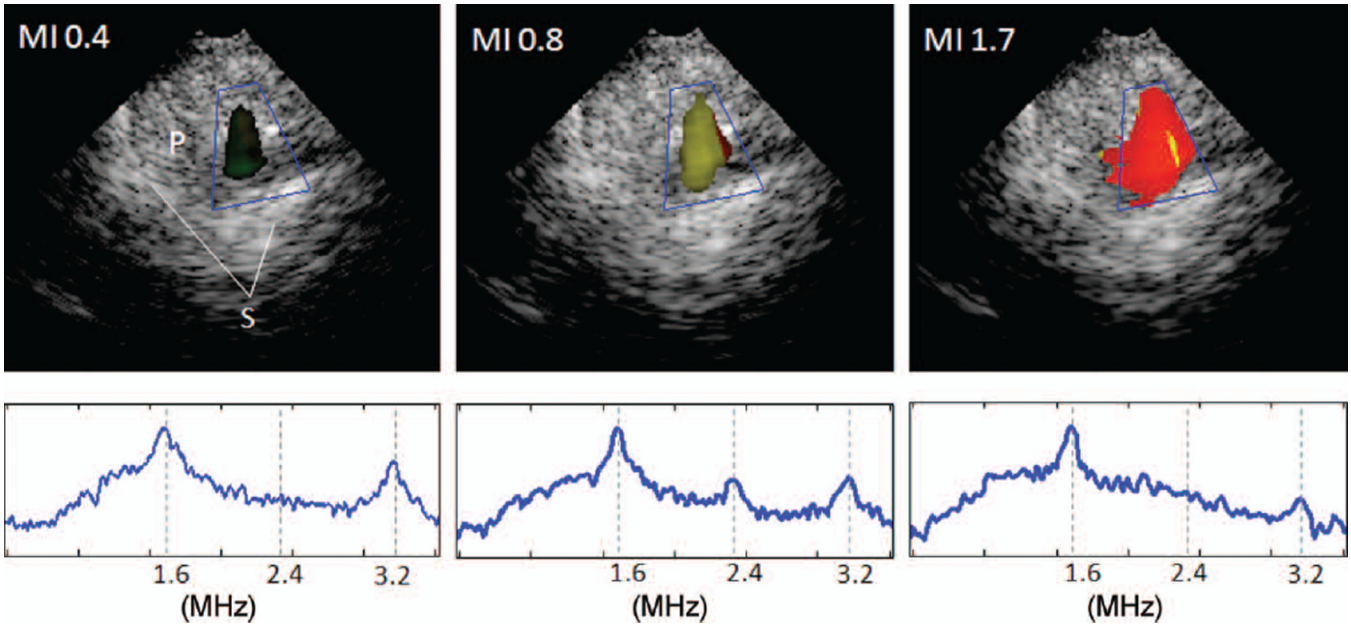

Fig. 7.

Cavitation images of a porcine brain through the temporal acoustic window at mechanical indexes (MIs) with dominant moderate oscillations (left), dominant stable cavitation (center), and dominant inertial cavitation (right), and the corresponding averaged spectra over the region of interest (inside the blue box). P = brain parenchyma, S = contralateral skull.

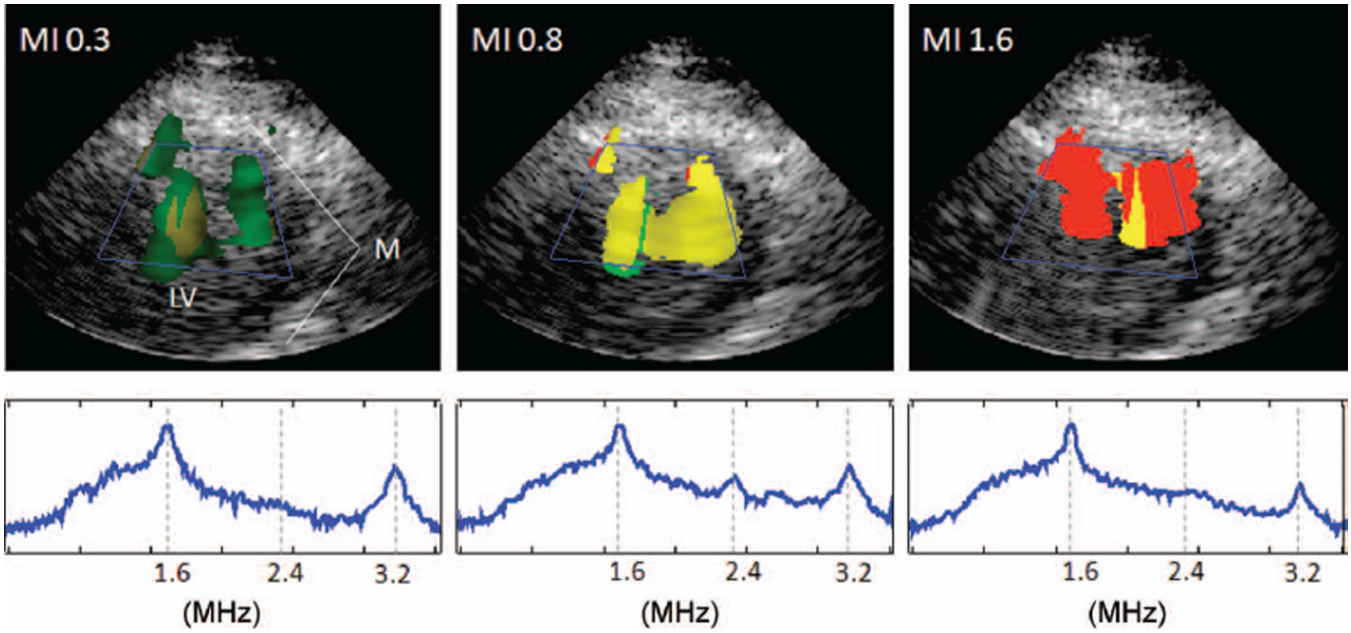

Fig. 8.

Cavitation images of a porcine heart (parasternal short-axis view of the left ventricle) at mechanical indexes (MIs) with dominant moderate oscillations (left), dominant stable cavitation (center), and dominant inertial cavitation (right), and the corresponding averaged spectra over the region of interest. LV = left ventricle, M = myocardium.

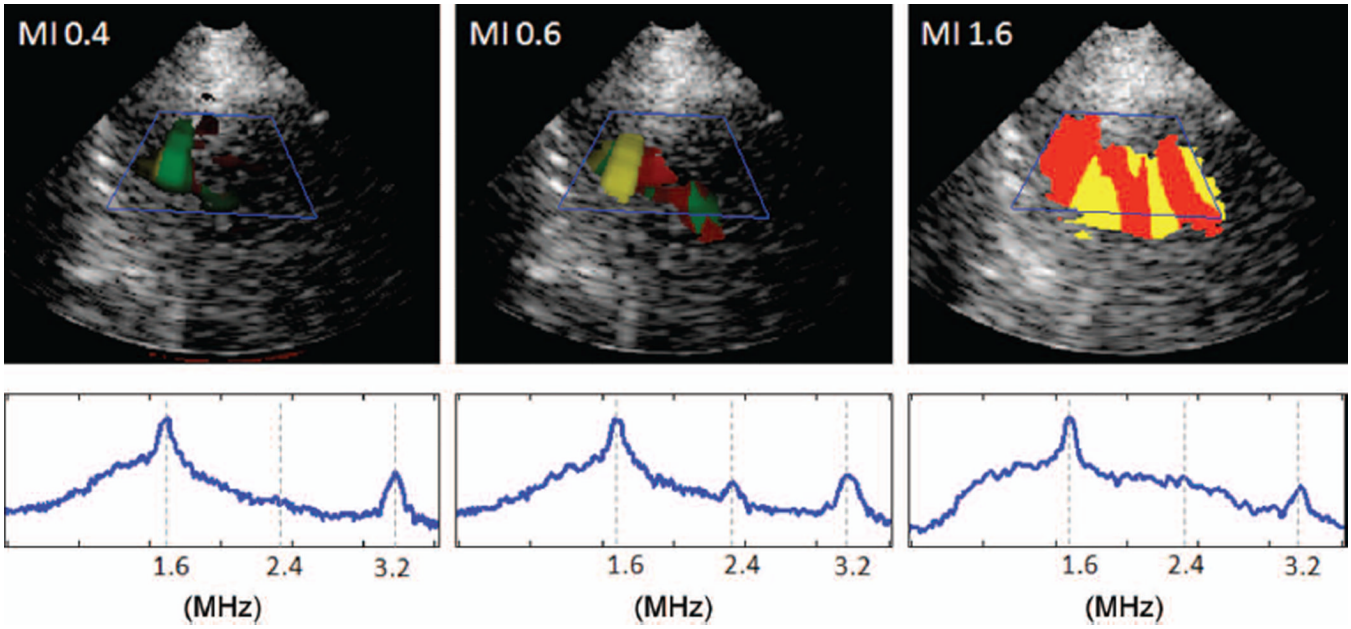

Fig. 9.

Cavitation images of a pig liver (subcostal view) at mechanical indexes (MIs) with dominant moderate oscillations (left), dominant stable cavitation (center), and dominant inertial cavitation (right), and the corresponding averaged spectra over the region of interest.

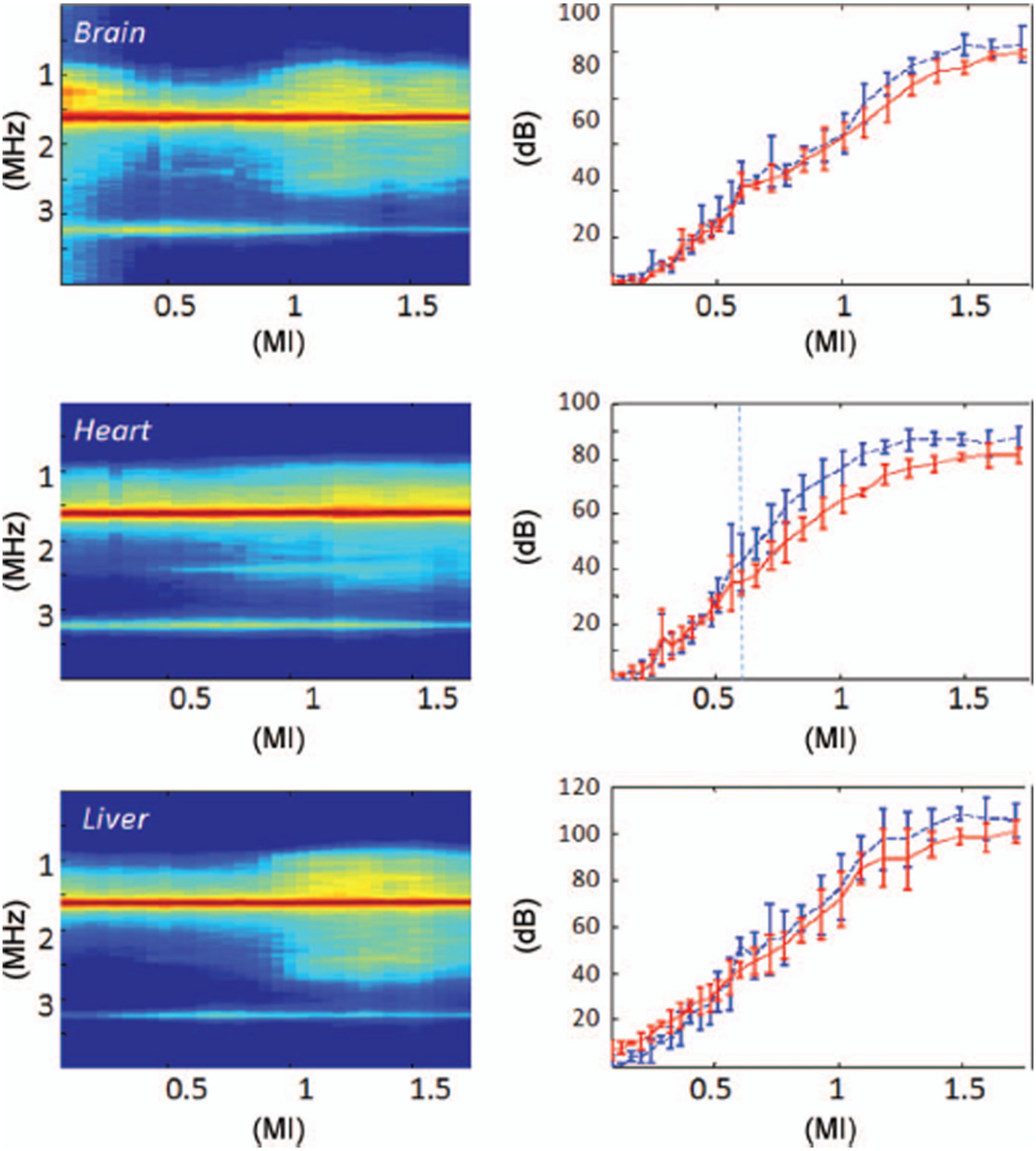

Fig. 10.

Averaged cavitation spectra (left) and cavitation doses (right) as a function of mechanical index (MIs) for the porcine brain (top), heart (middle), and liver (bottom). The same display is used here as in Fig. 6. The stable cavitation threshold can be readily identified from microbubbles within the heart chamber, but it is difficult to establish a threshold from the brain and liver examinations.